

## SUPPLEMENTARY INFORMATION

### Assessment of compressive Raman versus hyperspectral Raman for microcalcification chemical imaging

Camille Scotté<sup>1</sup>, Hilton B. de Aguiar<sup>2,\*</sup>, Didier Marguet<sup>3</sup>, Ellen Marie Green<sup>4</sup>, Pascaline Bouzy<sup>4</sup>, Sébastien Vergnole<sup>5</sup>, Charles Peter Winlove<sup>4</sup>, Nicholas Stone<sup>4</sup> and Hervé Rigneault<sup>1,\*</sup>

<sup>1</sup>Aix Marseille Univ, CNRS, Centrale Marseille, Institut Fresnel, Marseille, France

<sup>2</sup>Département de Physique, Ecole Normale Supérieure / PSL Research University, CNRS, 24 rue Lhomond, 75005 Paris, France

<sup>3</sup>School of Physics and Astronomy, University of Exeter, Exeter, UK

<sup>4</sup>Aix-Marseille Université, INSERM, CNRS, Centre d'Immunologie de Marseille-Luminy, Marseille, France

<sup>5</sup>HORIBA Scientific, Villeneuve d'Ascq, France

\*Corresponding authors: [h.aguiar@phys.ens.fr](mailto:h.aguiar@phys.ens.fr), [herve.rigneault@fresnel.fr](mailto:herve.rigneault@fresnel.fr)

---

This document provides supplementary information to “Assessment of compressive Raman versus hyperspectral Raman for microcalcification chemical imaging”. We provide more information about CRT theory, the instrumentation, the detectors characteristics, signal to noise ratio and limit of detection considerations, post-processing and the CRT experiment in the presence of background.

## A. CRT THEORY

We provide a brief overview of the mathematical method developed in (1) and focus on quantification (species proportions estimation). We assume a sample with spectrum  $y$  (measured over a certain frequency bandwidth  $v$  of  $K$  spectral bases) consists of a mixture of  $Q$  chemical species of known spectra  $S_i$ . Under a linear mixing assumption, we can write:

$$y(v) = \sum_{i=1}^Q z_i S_i(v) \quad (\text{S.1})$$

Where  $z_i$  are the unknown proportion coefficients.

Let  $M$  binary filters be sequentially displayed onto the DMD with  $M \geq Q$ . If the measurements are limited by Poisson noise (Fig. S-2), the measured number of photons  $n_m$  through filter  $F_m$  is modeled as a Poisson process ( $m = 1 \dots M$ ). For filter  $F_m$ , the mean number of measured photons  $\mu_m = \langle n_m \rangle$  is a projection of the filter  $F_m$  onto the sample spectrum  $y$  for a certain exposure time  $\tau_m$ :

$$\mu_m = \tau_m \sum_{k=1}^K F_m(v_k) y(v_k) \quad (\text{S.2})$$

Which, with equation (S.1), leads to

$$\mu_m = \sum_{i=1}^Q G_{mi} z_i \quad (\text{S.3})$$

(Or, in the matrix form:  $\boldsymbol{\mu} = \mathbf{G}\mathbf{z}$ ).

Where

$$G_{mi} = \tau_m \sum_{k=1}^K F_m(v_k) S_i(v_k) \quad (\text{S.4})$$

The two above equations state that the mean number of measured photons  $\mu_m$  is the projection of the filters  $F_m$  during time  $\tau_m$  onto the pure spectra  $S_i$  weighted with their relative proportion coefficients  $z_i$ .

### Filter design

To design the filters, we consider an unbiased estimator whose precision is given by the covariance matrix  $\boldsymbol{\Gamma} = \langle \delta \hat{\mathbf{z}} \delta \hat{\mathbf{z}}^T \rangle$ , where  $\hat{\mathbf{z}}$  is an estimation of  $\mathbf{z}$ ,  $\delta \hat{\mathbf{z}} = \hat{\mathbf{z}} - \langle \hat{\mathbf{z}} \rangle$  and  $^T$  is the transpose operation.

The  $M$  filters can then be determined in order to optimize a figure of merit deduced from  $\boldsymbol{\Gamma}$ . The figure of merit used in the algorithm in (1) is the trace of the Cramer-Rao lower bound (CRB) matrix. This CRB is a lower bound on the variance of any unbiased estimator and is given by (1):

$$[\mathbf{CRB}^{-1}]_{ij} = [\mathbf{I}_F]_{ij} = \sum_{m=1}^M \frac{G_{mi} G_{mj}}{\mu_m} \quad (\text{S.5})$$

Where  $\mathbf{I}_F$  is the information matrix. The above equation shows that the precision is a function of the binary filters, the proportions and the exposure time.

The implemented algorithm for filters design consists in a simple numerical optimization technique: a set of values  $(m, k)$  is randomly chosen and the value  $F_m(k)$  replaced by  $1 - F_m(k)$  if  $\text{trace}(\mathbf{CRB})$  is decreased.

The algorithm is similar to the one developed in (2). Indeed, our method minimizes the trace of the **CRB** while the method in (2) minimizes the trace of the covariance matrix  $\boldsymbol{\Gamma}$ . The two methods are equivalent for  $M = Q$ . It was indeed shown in (1)

that for  $M = Q$ ,  $= \mathbf{CRB}$ . Therefore, calculating the binary filters by minimizing the trace of the  $\mathbf{CRB}$  is equivalent to minimizing the mean square error of  $\hat{z}$  (trace of  $\mathbf{\Gamma}$  for an unbiased estimator).

However, the algorithms are quite different. In (1), the algorithm is a mean square error optimization problem under constraints, and both the filters and their respective exposures times are optimized. The optimization problem is nonlinear and nonconvex. In (3), the MATLAB function FMINCON is used to solve this problem (with no guarantee of finding the global minimum). In (2), other strategies are developed based on nearly binary filters.

On the other hand, in our approach, a simple numerical optimization technique is performed as described above, and the filters relative exposure times are constrained to be equal. This simple algorithm does not always guarantee convergence to global minimum, but simulations show that the precision reached with this method converges to values close to the CRB obtained with a full Raman spectrum (FRS) (i.e. best achievable precision for same number of photons), even for similar spectra (1). Furthermore, it was shown in (1) that optimizing the exposure times can lead to marginal improvement of the CRB, and no improvement when the filters are applied in parallel.

### **Proportion estimation**

Once the filters are designed and their projection on the mixture (S.1) completed, the estimation of the coefficients can be performed. When  $\mathbf{G}$  is not singular, the unknown proportion coefficients  $z_i$  can be retrieved from a simple linear estimation,

$$\hat{\mathbf{z}} = [\mathbf{G}^T \mathbf{G}]^{-1} \mathbf{G}^T \mathbf{n} \quad (\text{S.6})$$

In the case  $M = Q$  and when  $\mathbf{G}$  is invertible, (S.6) becomes  $\hat{\mathbf{z}} = \mathbf{G}^{-1} \mathbf{n}$ , and the linear method is efficient (1), i.e. unbiased  $\mathbf{z} = \langle \hat{\mathbf{z}} \rangle$  with precision equal to the CRB. It means that more complex estimators would not bring any precision improvement.

## **B. INSTRUMENTATION**

### **CRT setup**

The excitation light emitted by a CW 532 nm laser (Verdi, Coherent) is laser filtered (FLH532, Thorlabs) and focused onto the sample with a 20X/0.75 air objective (Nikon Instruments Inc.). The back-scattered light passes through a dichroic mirror (532 nm long-pass RazorEdge, Semrock) and is directed either into the CRT spectrometer, either into a commercial spectrometer (MicroHR, HORIBA) for validation. At the entrance of the CRT spectrometer, a notch filter (NF533-17, Thorlabs) blocks most of the Rayleigh light and a 100  $\mu\text{m}$  wide slit defines the active confocal volume of collected light. The latter is dispersed by 600l/mm grating (GR250608, Thorlabs) and focused onto the digital micromirror device (DMD) (V-7001, Vialux – 1024x768 active mirrors). The controllable DMD micro-mirrors (pixel size 13.7  $\mu\text{m}$ ) are fully vertically binned and horizontally binned (4 mirrors/pixel). Therefore the pattern displayed on the DMD is equivalent to a 1x256 matrix (the line size is 768 mirrors and one column size is 4 mirrors). Selected wavelengths signals are combined onto a single channel photo-multiplier tube (PMT) detector (H7421-40 photon counting module, Hamamatsu), so that the whole surface of the DMD is imaged onto the 5 mm detector active surface area.

Spectral calibration is conducted with a 594 nm He-Ne laser. Relay lenses (L3 to L7) are AR coated achromatic doublets (AC254-100-A-ML and AC254-150-A-ML, Thorlabs).

All samples were point scanned by a piezo stage at a speed of 4ms per pixel. The scheme of the setup is shown in Fig S-1 below.

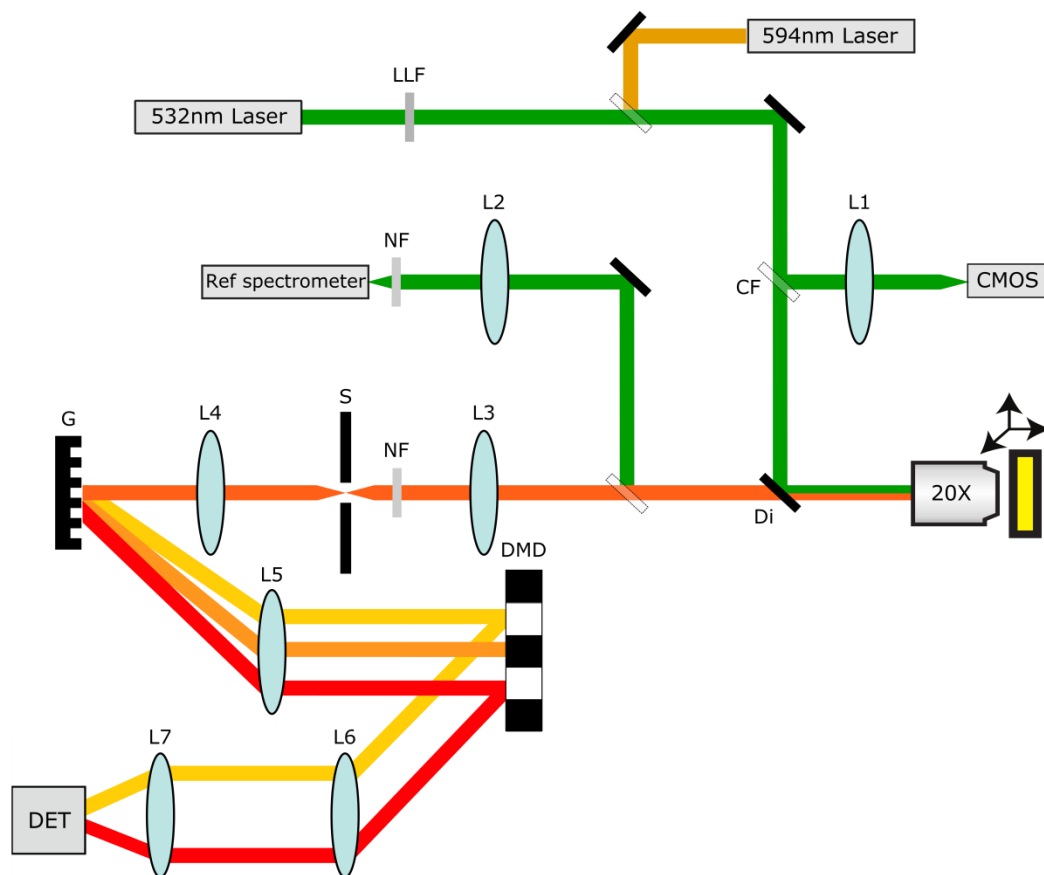


Figure S-1. Custom built CRT system setup. HeNe laser: 594nm laser for wavelength calibration; CMOS: for white light imaging (DCC1545M, Thorlabs); LLF: laser line filter; CF: cold filter mirror; G: grating; Di: Dichroic mirror; NF: notch filter; S: slit; DET: single channel detector. L1 and L2 are lenses to focus in the CMOS camera and in the reference spectrometer, respectively. L3:  $f=100\text{mm}$ , L4:  $f=100\text{mm}$ , L5:  $f=150\text{mm}$ , L6:  $f=150\text{mm}$ , L7:  $f=50\text{mm}$ . Silver mirrors are represented in black if fixed and in transparent if can be flipped.

### **Hyperspectral imaging experimental conditions**

The experiments on the WITec were conducted with an A/D rate of 33 kHz. This is not the fastest rate but was chosen to minimize the readout noise. In this mode, with optimized vertical clock speed, the minimum achievable integration time per spectra is 43 ms, regardless of the signal level. (Note that with the highest speeds of this CCD, one spectrum could be acquired in 12ms at the expense of a doubled readout noise). Thus, neglecting the retrace speed per line of the stage to scan the sample, one image of 100x100 pixels can be acquired in about 7 min at best in this low readout noise regime.

On the EMCCD with high EM gain, the readout noise is negligible so the chosen A/D rate on the HORIBA system is the fastest (3 MHz). The system was used in the fastest scanning mode. Cropping rows of the camera and using the fastest vertical clock speed, one spectrum could be acquired in about 2 ms. This is close to the maximal achievable speed of the device stated in the specifications. Thus, neglecting the retrace speed, one image of 100x100 pixels can be acquired in about 20 s at best in the chosen mode.

Table S-1 sums up the main specifications of the commercial Raman imaging (WITec and HORIBA) and of the custom-built CRT systems with their respective detectors (CCD DV401A-BV, Andor; EMCCD Synapse EM, HORIBA and PMT H7421-40 photon counting module, Hamamatsu). The values correspond to the study experimental conditions.

Table S-1. Main specifications of the three systems with their detectors

	WITec + CCD	HORIBA + EMCCD	CRT + Photon counting PMT
Spectral resolution	10 cm <sup>-1</sup>	20 cm <sup>-1</sup>	40 cm <sup>-1</sup>
Spatial resolution	0.38 μm	0.35 μm	1.4 μm
Pixel size	0.5 μm	0.6 μm	0.6-0.75 μm
Objective	50X / NA=0.7	50X / NA=0.75	20X / NA=0.75
Sensor	16 bits , BI cooled	16 bits , BI cooled	cooled
A/D rate	33 kHz	3 MHz	--
Vertical clock speed	16 μs	4.6 μs	--
Mode	Full vertical binning	SWIFT Crop mode (40 rows)	--
tpp	43 ms	2 ms	4 ms (limited by current scanning speed implemen- tation) <100 μs capability
Peak QE	95%	90%	40%
Conversion factor <i>g</i> (e-/count)	2.7	3.26	--
EM gain <i>g<sub>EM</sub></i>	--	999	--
Readout noise (e-/pixel)	(at 33 kHz) 2.25 counts (*) 6.1 e- (*)	(at 3 MHz) 34 counts (*) < 1e- (*)	--
Dark count (e-/pixel/sec)	0.006	<0.01	9 (*)

NA: numerical aperture; BI: back-illuminated; --: not applicable; tpp: integration time per spectrum; e-: electrons; (\*): experimentally measured values, see section C.

### C. DETECTORS CHARACTERIZATION

In this section we verify that CRT measurements are limited by photon noise. We also assess the detectors noise when no signal is recorded, which is relevant when performing measurements at low signal level and close to the detection limit of the three different systems.

#### CRT

CRT theory is based on the fact that the measured number of photons passing through a filter is a random variable satisfying a Poisson distribution when the measurements are limited by photon noise. We therefore need to check experimentally that our measurements are indeed limited by photon noise.

Let  $N$  be the number of counted photoelectrons by the detector. It is assumed to follow Poisson statistics so the variance of  $N$  should be equal to its mean,  $\sigma^2(N) = \langle N \rangle$ .

To check if the above hypothesis is verified, we count the photons detected through the system with a solution of DMSO as sample. On Fig S-2, the laser power is fixed to 100mW and the filter exposure time is varied between 50  $\mu$ s and 10 ms. Each experiment is repeated 2000 times. The curve shows that the standard deviation of  $N$  equals the square-root of its mean, which proves the  $N$  distribution follows Poisson statistics. The same relation is obtained with fixed exposure time and varying laser power.

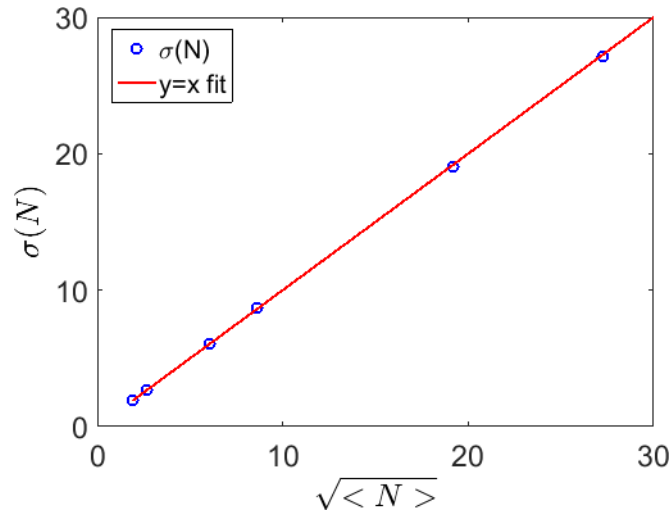


Figure S-2. Relation between the standard deviation of the measured number of photoelectrons  $N$  and the square-root of its mean, with fixed laser power (100 mW) and varying exposure time.

In addition, the dark noise (Poisson distributed and signal independent) is measured to ensure the dark noise level is negligible compared to the signals count rates in the scope of our studies. The dark noise level is measured in complete darkness. 1000 measurements were performed for each exposure time (varying between 50  $\mu$ s and 1 s). Figure S-3 shows the normalized histogram of dark counts for integration time 1 s. It can be fitted by a Poisson distribution of mean 8.56, which means the dark count of our detector is about of 9 photoelectrons per second. This value is low enough to ensure a negligible influence of the dark count on our measurements. Therefore, our measurements are limited by photon noise.

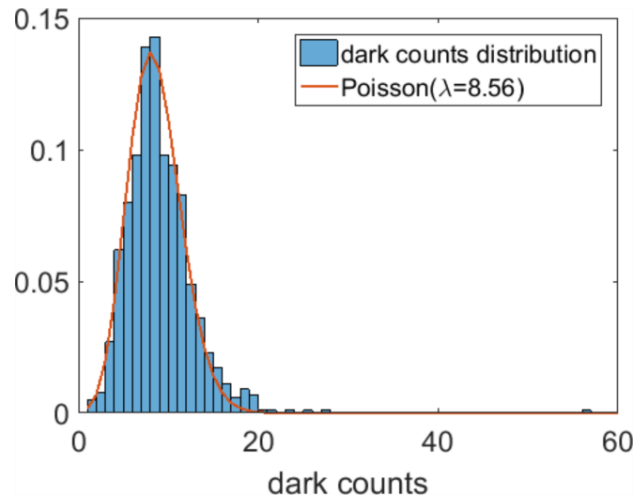


Figure S-3: Normalized histogram of the detector dark counts for 1 s exposure time, fitted with the probability density function of a Poisson distribution of parameter 8.56, giving an estimation of the detector dark noise.

### **Hyperspectral imaging cameras (CCD, EMCCD)**

Dark frames at minimum integration times of the WITec system CCD and HORIBA system EMCCD were acquired for electronic noise and baseline assessment. The dark frame measurements were performed under the same conditions as hyperspectral measurements (Table S-1).

The mean of the dark frame counts defines the baseline level, and the standard deviation the camera readout noise (signal independent noise). Figure S-4 shows the histograms of the signal recorded from the dark frames. Under the chosen modes, the CCD has a baseline level of about 712 counts and exhibits a Gaussian distributed readout noise of about 2.25 counts (6.1 electrons/pixel - see equation (S-13)). The EMCCD exhibits a Gamma distributed readout noise of about 34 counts (less than 1 electron/pixel - see equation (S-14)), with a baseline level of 34 counts. Our measurements were consistent with the manufacturer specifications. The baseline level is subtracted from all spectra before post-processing.

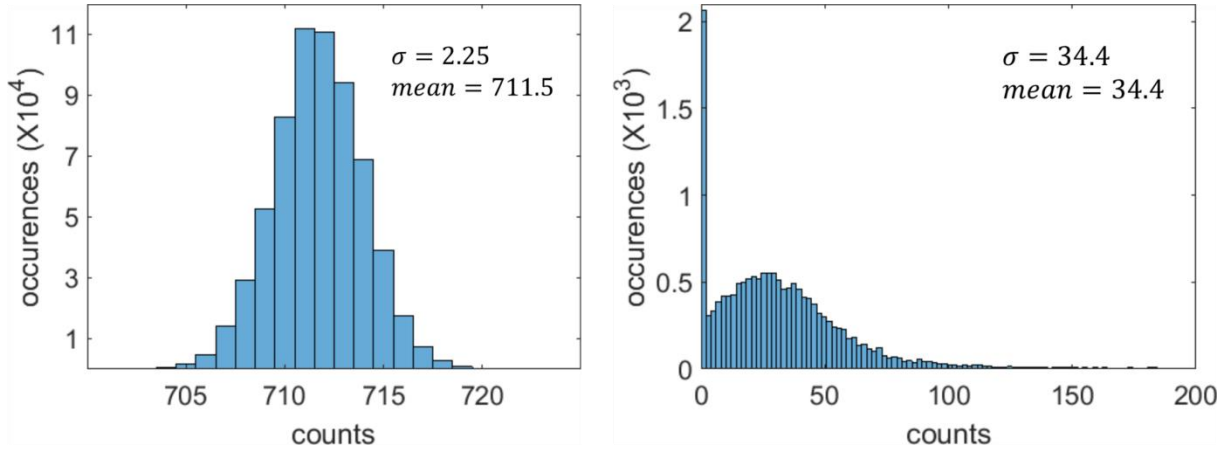


Figure S-4: Histograms of CCD (Left) and EMCCD (Right) dark frame. The standard deviation  $\sigma$  of the distribution corresponds to the readout noise and the mean to the baseline level.

#### **D. SIGNAL TO NOISE RATIO (SNR) AND LIMIT OF DETECTION (LOD) CONSIDERATIONS**

In this section, we discuss the SNR and LOD of the three systems.

In the first part dedicated to SNR, we precise what are the limited noise sources of the three detectors. We show only CRT is shot noise limited at all signal levels.

In the second part, we give details concerning the LOD calculations.

We first introduce the notations used throughout this section:

$N$ : Number of photons

$\Phi$ : Photon count rate (*photons/s*)

$\tau$ : Exposure time (*s*)

$QE$ : Detector quantum efficiency \*

$\sigma_s$ : Shot noise  $\sigma_s^2 = NQE\tau$  (*photoelectrons*)

$\sigma_{DN}$ : Detector dark-counts noise \* (*photoelectrons*)

$\sigma_R$ : Detector readout noise \* (*photoelectrons*)

$F$ : Excess noise factor (due to EMCCD multiplication register)

$g_{EM}$ : EMCCD EM gain \*

\*: values can be found in Table S-1.

##### **SNR analysis**

Table S-2 shows the theoretical expressions of the three detectors SNRs per pixel. We neglect clock-induced charge noise, fixed pattern noise, quantization noise and other potential sources of noise (5).

In the high signal regime, the CCD and PMT are shot-noise limited (intrinsic from photon detection), while the EMCCD has a contribution from the excess noise factor  $F$  (approximated to the value 1.4 (4)). However, our PMT only has 40% QE while the two cameras reach 90 to 95%. Therefore, the CCD shows an advantage on the CRT in the high photon number regime in terms of SNR/spectral pixel (Fig. S-5).

In the low signal regime, we consider integration times lower than about 10ms (relevant in the scope of the paper). In this regime, the CCD is limited by its readout noise. The EM gain was set to 999, making the EMCCD readout noise negligible and leading to the same expression as in the high signal regime. Last, we showed that the CRT experiments were shot noise limited (Fig S-2).

Therefore, CRT is shot-noise limited regardless of the signal level, as opposed to the two other detection strategies. Although the CRT brings a great advantage over the CCD hyperspectral imaging in the low signal regime, it would benefit from a single pixel detector with higher quantum efficiency (e.g. avalanche photodiode). This is possible if the way the signal is focused

into the detector is revised, due to the small active area of avalanche photodiodes. However, at equal SNR, we remind CRT is faster than hyperspectral imaging.

Table S-2. Theoretical SNR per pixel of the three detectors.

	$SNR_{CCD}$	$SNR_{EMCCD}$	$SNR_{PMT}$
General expression	$\frac{\Phi QE \tau}{\sqrt{\sigma_s^2 + \sigma_{DN}^2 + \sigma_R^2}}$	$\frac{\Phi QE \tau}{\sqrt{F^2(\sigma_s^2 + \sigma_{DN}^2) + \left(\frac{\sigma_R}{g_{EM}}\right)^2}}$	$\frac{\Phi QE \tau}{\sqrt{\sigma_s^2 + \sigma_{DN}^2}}$
High signal $\Phi\tau$	$\sqrt{\Phi QE \tau}$	$F^{-1} \sqrt{\Phi QE \tau}$	$\sqrt{\Phi QE \tau}$
Limit for the considered detectors at high signal	$0.97 \sqrt{\Phi \tau}$	$0.67 \sqrt{\Phi \tau}$	$0.63 \sqrt{\Phi \tau}$
Low signal $\Phi\tau$	$\frac{\Phi QE \tau}{\sigma_R}$	$F^{-1} \sqrt{\Phi QE \tau}$	$\sqrt{\Phi QE \tau}$

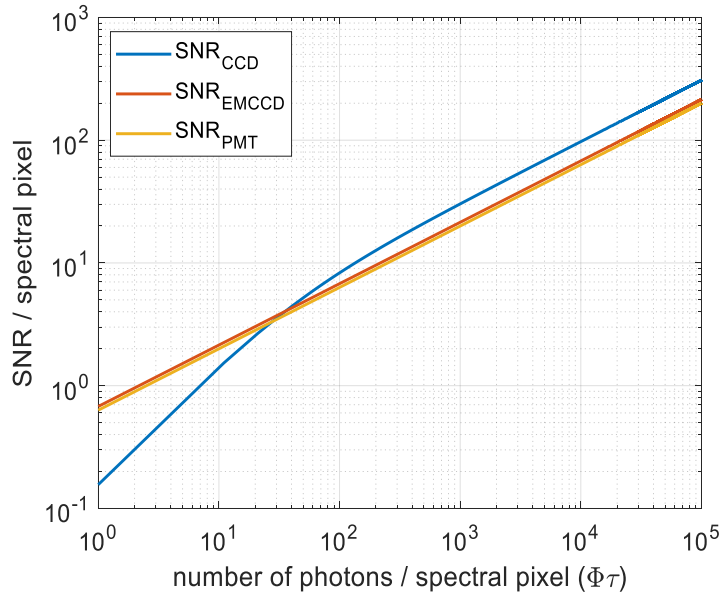


Figure S-5: SNR per spectral pixel of the three detectors as a function of the signal level (number of photons), with  $\Phi = 10^4 \text{ photon} \cdot \text{s}^{-1}$  and  $\tau \in [10^{-4}; 10] \text{ s}$ .

The above analysis shows the limiting noises of the three detectors. However, this analysis is limited since it does not take into account their different detection schemes: in the camera-based systems, the signal is distributed over the cameras pixels, whereas CRT combines relevant spectral components into a single pixel.

For instance, consider a hypothetical signal dispersed over 20 spectral pixels of interest. From figure S-5, we see that to reach a SNR/pixel of 1, the number of photons per spectral pixel is about 7 for the CCD, 2 for the EMCCD and 3 for the PMT. Then, to reach a SNR/pixel of 1 in every spectral pixel, the CCD needs in total about 140 photons (7x20), the EMCCD 40 photons, and the CRT 3 photons (because it recombines all the wavelengths into one pixel).

Therefore, in the low signal level limit, we choose to compare the systems limits of detection (LOD):

We define the LOD as the minimal Raman signal (integrated over all wavelengths) that must arrive on the detector to be able to achieve species proportion estimation. This photon budget is either dispersed on 1024 spectral pixels (cameras), either recombined after filter projection into 1 pixel (CRT). To be clear, we wish to find the minimal photon budget necessary to achieve proportion estimation for each of the three techniques, theoretically and for our experiments.



## LOD analysis and discussion

To gain insight of the three techniques LOD, we performed experiments decreasing gradually the laser power on the sample. The closest experiment to the LOD is the last experiment until the SNR is too low for proportions to be estimated. The LOD values we calculate are then upper bounds on the LOD.

For example, on the EMCCD system, we acquired the reference spectrum of HAP, COM and CaF<sub>2</sub> and calculated the corresponding binary filters (Fig.S-6). Only the filters corresponding to HAP and COM are represented in the figure. We projected the filters corresponding to HAP and COM on the hyperspectral data cube obtained after point scanning the image. An average of the spectra close to the LOD is shown in (Fig.S-6). On average, projecting the filters on HAP-COM pixels close to the LOD gives an approximation of the LOD for this example. The number of photons  $N_{tot}$  is deduced from the number of counts with equations (S-13) and (S.14).

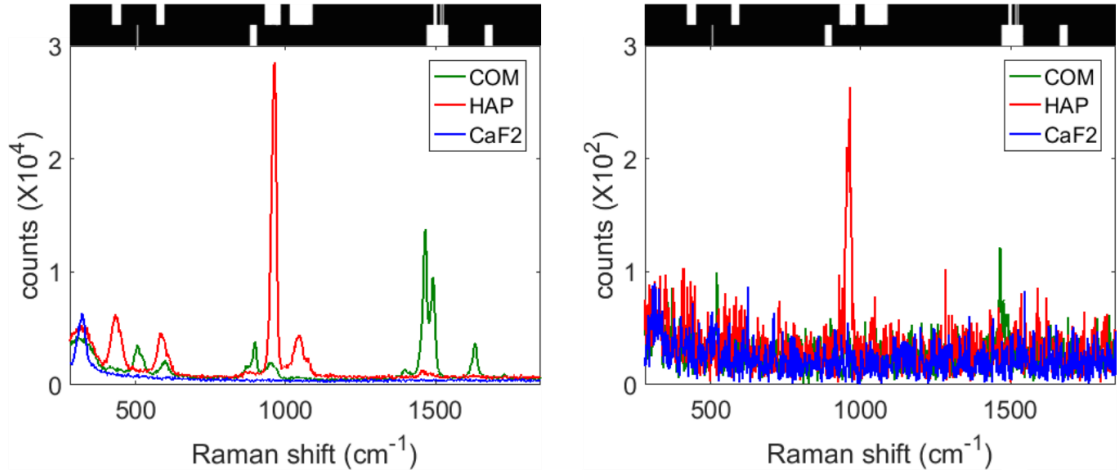


Figure S-6: Left: COM, HAP and CaF<sub>2</sub> reference spectra acquired with the EMCCD system (averaged on 20 spatial pixels). From those spectra, binary filters are generated. Only the filters corresponding to HAP and COM are represented. Right: Same spectra close to the system LOD. Projecting the filters on the spectra on every image pixel gives the LOD approximation for this example.

On figure S-7 and S-8 below we plot the spectra at the estimated LOD for HAP-COM (Fig S-7, related to Fig.4 of the main text) and HAP-CHAP (Fig S-8, related to Fig.5 of the main text).

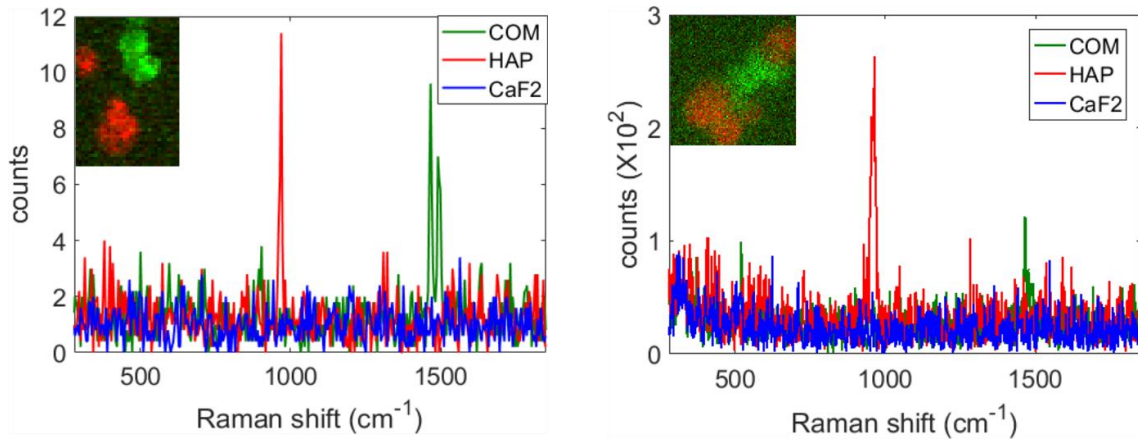


Figure S-7: Average spectra ( $\sim 20$ ) of COM, HAP and CaF<sub>2</sub> at the estimated LOD for the CCD-based system (left) and the EMCCD-based system (right).

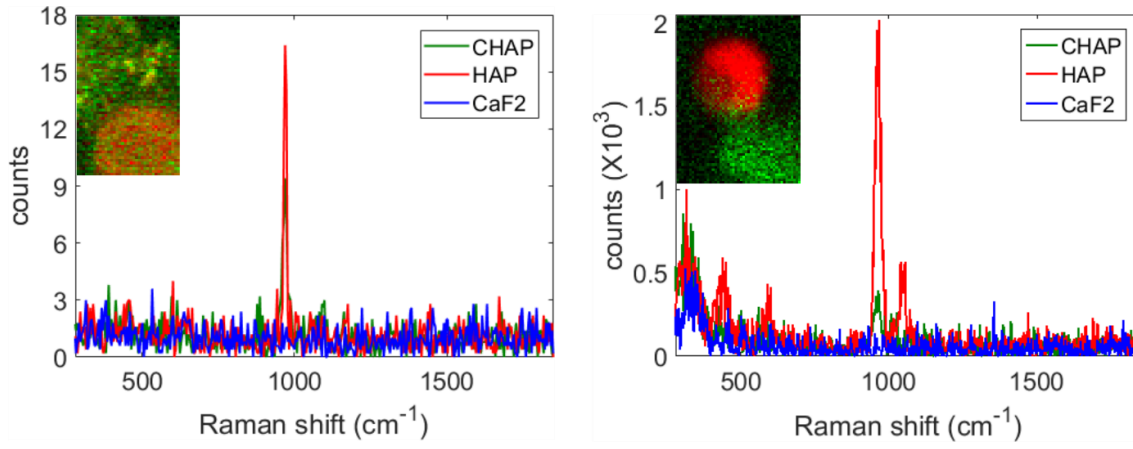


Figure S-8: Average spectra ( $\sim 20$ ) of CHAP, HAP and  $\text{CaF}_2$  at the estimated LOD for the CCD-based system (left) and the EMCCD-based system (right).

On the table below, we relate the LOD to the SNR at a decisive spectral pixel for chemical quantitation (We remind the LOD is the minimal signal level at which quantitation is successful). In a simple model, this spectral pixel is the most chemically specific peak that allows species discrimination. We name this spectral pixel “decisive” pixel. We chose this simplified model because if the signal on this spectral pixel is buried into the camera noise, quantitation is expected to fail. In our example we estimate this pixel to be the COM peak at  $1500\text{cm}^{-1}$  (for HAP-COM - see Fig. S-7) and the CHAP peak at  $1071\text{cm}^{-1}$  (for HAP-CHAP - see Fig. S-8). For CRT, we directly use the  $N_{\text{tot}}$ . The SNRs per spectral pixel are calculated from Table S-2 (low photon regime).

From this table, we see that:

- The LOD is probably overestimated for the CCD in the HAP-COM case because of the high SNR found (3.64). We found that for  $N_{\text{tot}}=150$  (SNR=1.33) we couldn’t distinguish the HAP and COM species.
- CRT LOD is also probably overestimated. However CRT LOD is already lower than the hyperspectral cases.

Table S-3: Estimated LOD and SNR associated with figures 4 and 5.

	WITec + CCD	HORIBA + EMCCD	CRT + PMT
<b>Figure 4 (HAP-COM)</b>			
LOD upper bound ( $N_{\text{tot}}$ photons)	450	40	15
Signal at “decisive” pixel * (photons)	23 (8counts)	1 (100counts)	15
SNR at “decisive” pixel **	$23 \times QE/6 = \mathbf{3.64}$	$\sqrt{1 \times QE}/1.4 = \mathbf{0.67}$	$\sqrt{15 \times QE} = \mathbf{2.44}$
<b>Figure 5 (HAP-CHAP)</b>			
LOD upper bound ( $N_{\text{tot}}$ photons)	1000	250	20
Signal at “decisive” pixel * (photons)	9 (3counts)	1 (200counts)	20
SNR at “decisive” pixel **	$9 \times QE/6 = \mathbf{1.43}$	$\sqrt{1 \times QE}/1.4 = \mathbf{0.67}$	$\sqrt{20 \times QE} = \mathbf{2.83}$

\*: Camera-based systems: signal at the “decisive” spectral peak for proportion estimation (Figure 4: COM peak at  $1500\text{cm}^{-1}$  – Figure 5: CHAP peak at  $1071\text{cm}^{-1}$ ). Those signal levels are read from figures S-7 and S-8 and converted from counts to photons with equations (S-13) for the CCD system and equation (S-14) for the EMCCD system. CRT:  $N_{\text{tot}}$  values.

\*\* : values calculated from Table S-2 (low signal regime)

## E. FROM RAW IMAGES TO RGB IMAGES

### CRT photon counts images

In CRT, the raw data after point scanning consists of images in which pixels represent the number of detected photons. One image per projected filter is obtained. Figure S-5 shows the two images after projection of the filters on the beads samples (polystyrene PS and melamine resin MR). F2 is mainly selecting PS resonances so more signal is detected on the PS bead (Right image). F1 is mainly selecting MR resonances, but since MR gives lower Raman signal than PS and since their resonances partially overlap, no noticeable difference in photon counts can be seen after F1 projection (Left image).

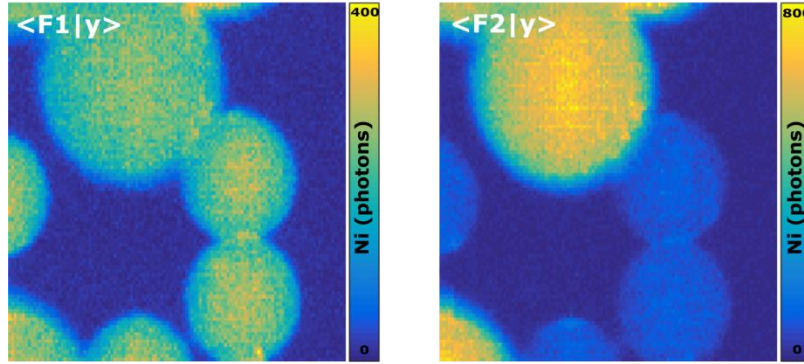


Figure S-9. Example of counted photons maps after filters projection on every pixel of the image for melamine resin (MR) and polystyrene (PS) beads. Left: image recorded after projection of F1 on every pixel. Right: image recorded after projection of F2 on every pixel.

### Proportion coefficients maps and RGB images

From the raw data, estimation of proportion is performed on every pixel of the region of interest to obtain proportion coefficient maps. Proportion coefficients maps in the paper represent the raw estimated proportions coefficients  $\hat{z}_i$  constrained to the interval  $[0, 1]$ .

For contrast purposes, the RGB images were obtained by normalizing the raw estimated proportion coefficients  $\hat{z}_i$  in each map to the maximum pixel value of the map. That is to say, on the proportion map  $k$ , the values of pixels  $i$  were normalized as follow:

$$\hat{z}_{k,i}^n = \hat{z}_{k,i} / \max_{j \in \text{map } k} (\hat{z}_{k,j}) \quad (\text{S.7})$$

The RGB images were obtained on each pixel  $i$  with:

$$\hat{z}_i^{RGB} = (\hat{z}_{1,i}^n, \hat{z}_{2,i}^n, 0) \quad (\text{S.8})$$

The same above constraints are applied for all proportion maps and RGB images of both CRT and conventional hyperspectral imaging.

## F. METHOD FOR CALCULATING $N_{tot}$

### CRT

If a set of  $Q$  filters is projected, the raw data is composed of  $Q$  images  $j$ , with value on pixel  $i$ :

$$n_{i,j} = \mathbf{F}_j \mathbf{y}_i \quad (\text{S.9})$$

So the total number of photons detected per pixel is:

$$N_i = \sum_{j=1}^Q n_{i,j} \quad (\text{S.10})$$

Finally, the average total number of photons we are interested in is the average of  $N_i$  on species pixels:

$$N_{tot} = \langle N_i \rangle_{species\ pixels} \quad (S.11)$$

### **Hyperspectral imaging**

We want to compare the signal at the limit of detection in CRT and in hyperspectral imaging. To do so, we use the reference spectra  $\mathbf{S}$  measured with the conventional spectrometers and generate the corresponding filters with our algorithm. We then project them on the hyperspectral data cube (Fig.S-6).

The output of this procedure is a data composed of  $Q$  images as in CRT, except the pixels are in units of counts. And the total number of counts on species pixels is deduced as above:

$$N_{tot}^{counts} = \langle N_i^{counts} \rangle_{species\ pixels} \quad (S.12)$$

For CCD, the corresponding number of photons can be obtain by multiplying the number of counts by the conversion factor  $g$  (in units of electrons/count) divided by the quantum efficiency  $QE$

$$N_{tot} = \frac{N_{tot}^{counts} g}{QE} \quad (S.13)$$

For EMCCD, quantification of the incoming signal is not precise due to the probabilistic nature of the multiplication process. We nevertheless obtain an order of magnitude by multiplying the number of counts by the conversion factor  $g$  divided by the quantum efficiency and EM gain  $g_{EM}$  (in units of counts/electron) :

$$N_{tot} = \frac{N_{tot}^{counts} g}{QE g_{EM}} \quad (S.14)$$

### **G. HYPERSPERICAL IMAGING: SPECTRA FOR PROPORTION ESTIMATION**

In this section we show the reference spectra used for estimating the proportion coefficients maps obtained with the hyperspectral imaging systems. We also show the spectra and RGB images with the EMCCD based system just above and below the limit of detection.

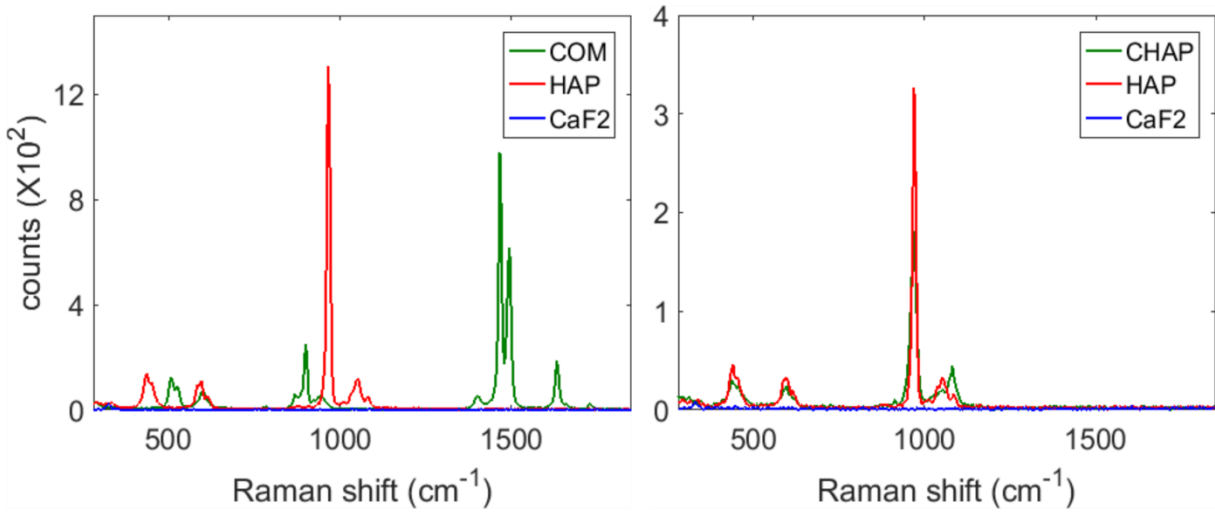


Figure S-10: Reference spectra (COM, HAP, CHAP, CaF2 background) for proportion estimation obtained with the WITec system equipped with CCD. The spectra are averaged over 20 spectra acquired with full laser power (16mW) on sample and for an exposure time of 43ms.

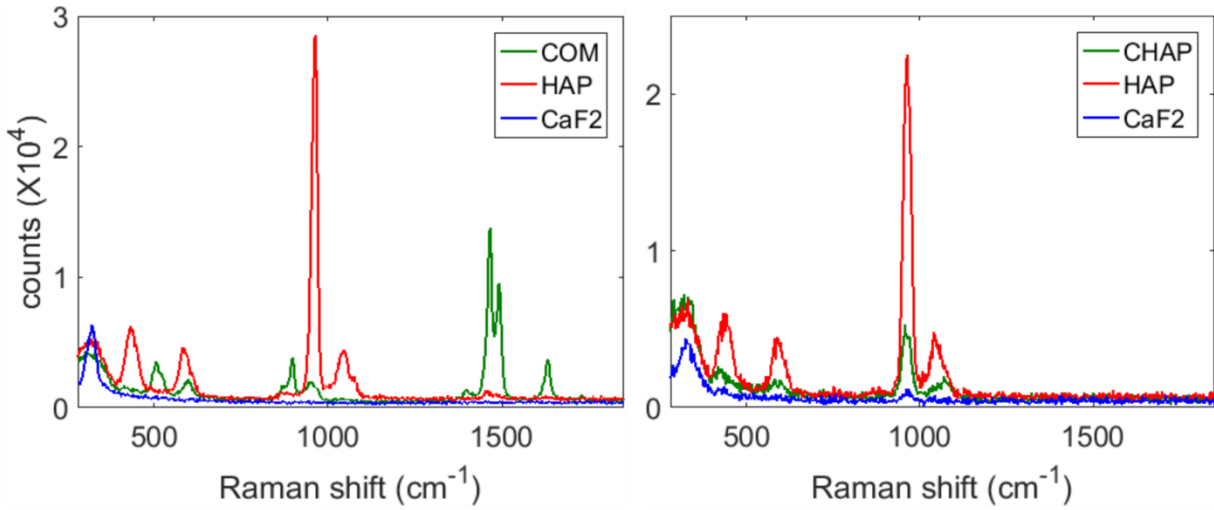


Figure S-11: Reference spectra for proportion estimation (COM, HAP, CHAP, CaF<sub>2</sub> background) obtained with the HORIBA system equipped with EMCCD. The spectra are averaged over 20 spectra acquired with full laser power (40mW) on sample and for an exposure time of 2ms.

## H. CRT EXPERIMENTS ON CHICKEN BREAST TISSUE BACKGROUND

In this section we give more details about the CRT experiment conducted in a presence of chicken breast tissue. This experiment was conducted to show an example of CRT in presence of a tissue background. We placed a 1 mm piece of chicken breast on a glass coverslip. We then sprinkled microcalcifications powders (COM and HAP) on the chicken tissue and push with a coverslip that we afterwards withdraw. Because of the highly scattering nature of this tissue, it is hard to know where the samples are in the microscope field of view. Thus, we did not acquire COM and HAP spectra in this new sample, rather we decided to explore three different strategies:

- A. We do not proceed to any learning step on the sample. Since we had done the experiment with the same samples on a CaF<sub>2</sub> coverslip without chicken breast (Fig.3 c-d), we simply project the filters that were already generated. We use only the same 2 filters as in Fig.3 c.
- B. Same as in A., but with filters generated with the background from CaF<sub>2</sub>
- C. We acquire the spectrum from the tissue (0.1 s integration time averaged on 4 spatial points) and take it into account with the previously acquired spectra of COM and HAP to generate the filters set (Fig.3 e).

Fig. S-12 shows the reference spectra, generated filters, proportion maps and RGB images for the three strategies A, B and C. On the RGB images, COM is represented in green, HAP in red and the chicken breast tissue in blue. The field of view is made of a large piece of COM powder on tissue, with some HAP on top of the COM.

**Strategy A** with no background consideration was performing well with no tissue (Fig.3 d) but here cannot differentiate tissue from HAP. This was foreseeable since we wish to discriminate three species with only two filters.

**Strategy B** performs well in estimating the proportions though the tissue spectrum was not considered: The filter corresponding to CaF<sub>2</sub> is distributed all over the spectral range (Fig. S-12 e) captures most of the tissue signal. However, on the proportion maps of HAP (f) and COM (g), the tissue proportion is not zero as it should be.

**Strategy C** performs the best, with zero tissue proportion on the HAP and COM proportion maps (k, l). Note that the filters are different that in B. We also see more details that with strategy B: On the top right of the field of view, there seems to be a HAP hidden below the tissue that only strategy C captures.

With this example we want to highlight that CRT is a background adaptable technique. The filters are optimized in a different way depending on the background. The algorithm takes into account the background to probe the best wavelengths and still be able to retrieve the proportions of the species of interest. In this example, we consider the background as a species. But for further improvement, we could also take into account the fact it is just background and not a species of interest like in (6). We think it is an interesting advantage over standard hyperspectral imaging in which the same information is measured whatever is the background and in which the background presence can only be post-processed.

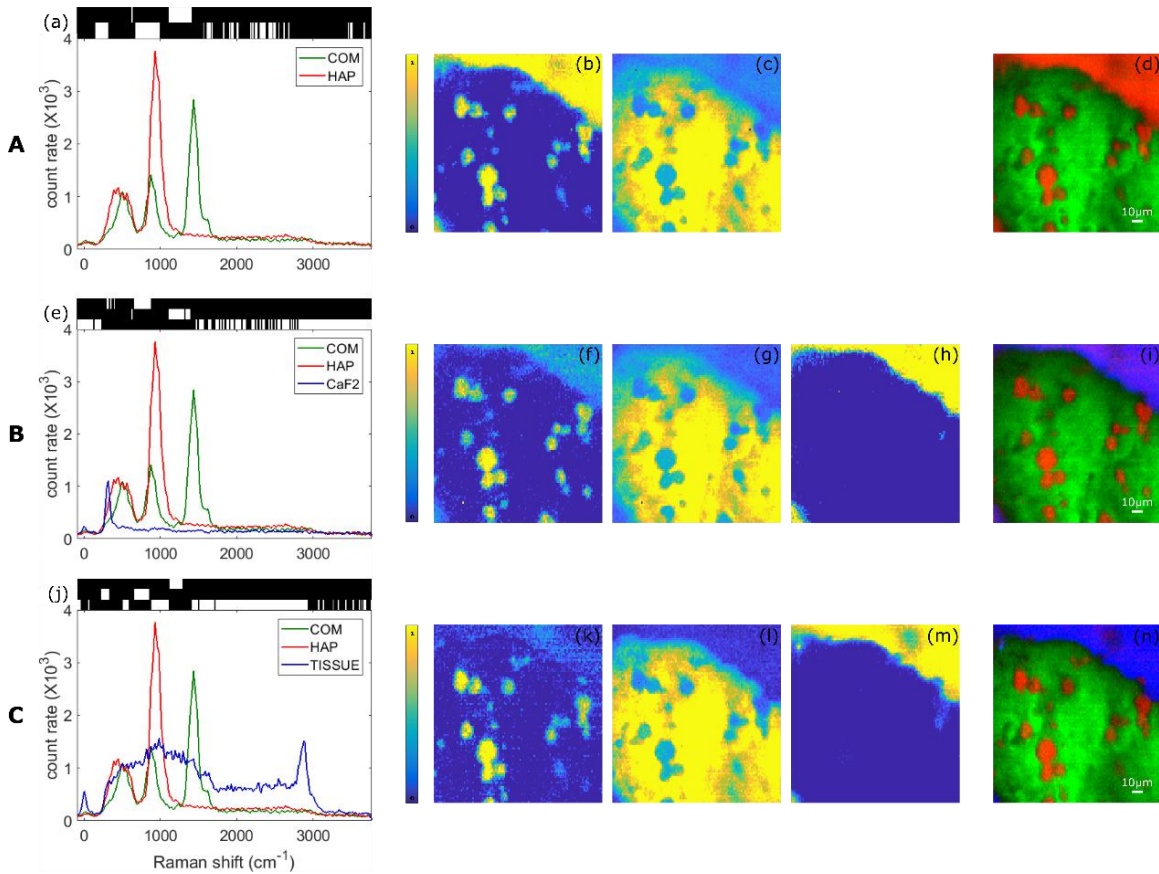


Figure S-12: (a): COM and HAP reference spectra - learnt with the samples powders on  $\text{CaF}_2$  substrate- and the 2 calculated filters. (b)-(c): Proportion maps estimated after filters projection. HAP and tissue cannot be distinguished. (d): associated RGB image. (e): COM, HAP and  $\text{CaF}_2$  reference spectra - learnt with the powders on  $\text{CaF}_2$  - and the 3 calculated filters. (f)-(h): Proportion maps estimated after filters projection of HAP (f), COM (g) and tissue (h). The species are distinguished but small proportions of HAP and COM are estimated where only tissue stands. (i): associated RGB image. (j): COM and HAP reference spectra - learnt with the powders on  $\text{CaF}_2$  - and the tissue reference spectra. Top: the 3 calculated filters. (k)-(m): Proportion maps estimated after filters projection of HAP (k), COM (l) and tissue (m). The species are distinguished with better accuracy than with strategy B. (n): associated RGB image.

## REFERENCES

1. Réfrégier, P.; Scotté, C.; De Aguiar, H. B.; Rigneault, H.; Galland, F. *J. Opt. Soc. Am. A*. **2018**, 35, 125-134
2. Buzzard, G. T.; Lucier, B. J. *Computational Imaging*. **2013**, 865707.
3. Wilcox, D. S.; Buzzard, G. T.; Lucier, B. J.; Wang, P., and Ben-Amotz, D., *Anal. Chim. Acta*. **2012**, 755, 17-27.
4. Robbins, M. S.; Member, S.; Hadwen, B. J. *IEEE Trans. on Electron Devices*. **2003**, 50.5, 1227-1232.
5. Konnik, M. and Welsh, J., 2014. *arXiv preprint arXiv:1412.4031*.
6. Rehrauer, O.G.; Mankani, B.R.; Buzzard, G.T.; Lucier, B.J.; Ben-Amotz, D. **2015**, *Opt. Express*, 23(18), pp.23935-23951.